

Outlier classification using Autoencoders: application for fluctuation driven flows in fusion plasmas

R. Kube* and F. M. Bianchi

Department of Physics and Technology, UiT The Arctic University of Norway, N-9037 Tromsø, Norway

D. Brunner

Commonwealth Fusion Systems, Cambridge, MA, USA

B. LaBombard

MIT Plasma Science and Fusion Center, Cambridge, MA, 02139, USA

(Dated: October 29, 2021)

Understanding the statistics of fluctuation driven flows in the boundary layer of magnetically confined plasmas is desired to accurately model the lifetime of the vacuum vessel components. Mirror Langmuir probes (MLPs) are a novel diagnostic that uniquely allow to sample the plasma parameters on a time scale shorter than the characteristic time scale of their fluctuations. Sudden large-amplitude fluctuations in the plasma degrade the precision and accuracy of the plasma parameters reported by MLPs for cases in which the probe bias range is of insufficient amplitude. While some data samples can readily be classified as valid and invalid, we find that such a classification may be ambiguous for up to 40% of data sampled for the plasma parameters and bias voltages considered in this study. In this contribution we employ an autoencoder (AE) to learn a low-dimensional representation of valid data samples. By definition, the coordinates in this space are the features that mostly characterize valid data. Ambiguous data samples are classified in this space using standard classifiers for vectorial data. This way, we avoid to define complicate threshold rules to identify outliers, which requires strong assumptions and introduce biases in the analysis. Instead, these rules are learned from the data by statistical inference. By removing the outliers that are identified in the latent low-dimensional space of the AE, we find that the average conductive and convective radial heat flux are between approximately 5 and 15% lower as when removing outliers identified by threshold values. For contributions to the radial heat flux due to triple correlations, the difference is up to 40%.

I. INTRODUCTION

Tokamaks confine fusion plasmas, a fully ionized hydrogen plasma with a core temperature of approximately 100,000,000 K, using strong, donut-shaped magnetic fields within a vacuum vessel¹. The outer boundary region of the plasma comprises a region where closed magnetic field lines wind around toroidal surfaces and a region where open magnetic field lines are guided as to intersect material walls, so-called divertor targets, remote from the central plasma column. As plasma streams along the open field lines onto the divertor targets, it cools. These field lines terminate at divertor structures which facilitate the further removal of the plasma. Thereby this region defines an exhaust channel for the plasma. Intermittent, large-amplitude fluctuations of the plasma parameters, such as the density and the temperature, are characteristic for the outboard mid-plane open field line region²⁻⁶. These fluctuations are foot prints of coherent structures of excess plasma pressure, called blobs, which propagate radially out over through the open field line region onto the vacuum vessel walls at the outboard mid-plane⁷⁻¹¹. Depending on their amplitude, these fluctuations can potentially erode the vacuum vessel. Impurities released from the wall may furthermore accumulate within the confined plasma column and negatively impact the confinement properties of the plasma. Today's tokamaks perform experiments on plasma discharges which last for several seconds. Future fusion reactors need to operate with long pulses or continuously. In order to model the life time of the plasma facing components for such requirements, a precise and accurate description of this fluctuation driven transport is desired^{12,13}.

Langmuir probes are the workhorse used to diagnose this boundary region plasma. They are implemented as electrodes immersed into a plasma. Using electric current and voltage samples recorded by a Langmuir probe, plasma quantities are recovered from the relation¹⁴

$$I_{\text{pr}} = I_{\text{sat}} \left[1 - \exp \left(\frac{V_{\text{pr}} - V_{\text{f}}}{T_{\text{e}}} \right) \right]. \quad (1)$$

Here I_{pr} is the collected electric current and V_{pr} applied bias voltage. T_{e} gives the electron temperature of the plasma. The floating potential V_{f} is defined as the electric potential assumed by an electrically isolated object were it to be immersed into the sampled plasma. The ion saturation current I_{sat} is the maximal current that can be drawn by an electrode, which is limited by ion collection of the electrode.

In order to estimate the particle and heat fluxes driven by the electric drift, the electron density, temperature, and the local electric field need to be recovered from probe measurements. Commonly, these quantities are recovered from probes by applying a sweeping voltage to the electrode. This allows to sample several current-voltage measurements ($I_{\text{pr}}, V_{\text{pr}}$) during one sweep. From these, I_{sat}, T_e and V_f are obtained from a fit on Eq.(1). The ion saturation current and the electron temperature can be used to calculate the electron density of the plasma as¹⁴

$$n_e = 2 \frac{I_{\text{sat}}}{e A_p \sqrt{k_b T_e / m_i}}. \quad (2)$$

Here e is the elementary charge, A_p is the current collecting area of the electrode, k_b is the Boltzman constant, and m_i denotes the ion mass. The electric potential in the plasma can be estimated as

$$V_p = V_f + \Lambda T_e, \quad (3)$$

where $\Lambda \approx 2 - 3$ for scrape-off layer plasmas^{15,16}. Potential measurements from poloidally separated electrodes allow to estimate the poloidal electric field, which drives the radial electric drift.

A characteristic time scale for fluctuations of $n_e, T_e,$ and V_p in boundary plasma is given by approximately $10\mu\text{s}$ ^{6,17-24}. Sweeping the voltage with a frequency larger than approximately 100 kHz however leads to hysteresis effects in the sampled current-voltage characteristic as the bias voltage polarizes the flux tube that plasma is sampled from^{25,26}. Thus, Langmuir Probes used in this manner can not sample the plasma parameters on a fast enough time scale to resolve the fluctuations of the boundary layer plasma.

The Mirror Langmuir probe (MLP) biasing technique allows to sample $I_{\text{sat}}, T_e,$ and V_f on a time scale below that of the boundary layer plasma fluctuation^{27,28}. The MLP diagnostic consists of three main components. The actual mirror Langmuir probe is an electric circuit outputs a current-voltage (I-V) characteristic with three adjustable parameters $I_{\text{sat}}, T_e,$ and V_f , given by Eq.(1). The second main component is a Langmuir electrode immersed in the plasma. Both components are connected to a fast switching biasing waveform, the third main component of the MLP diagnostic. The bias waveform switches between the states (V^+, V^0, V^-), such that the Langmuir electrode draws approximately $\pm I_{\text{sat}}$ at the states V^\pm and zero net current when biased to V^0 , as shown in Fig. 1 of²⁸. The target bias voltage state is updated every 300 ns. Once the bias voltage has settled, the current drawn from the MLP and the Langmuir electrode are sampled. The ion saturation current, the plasma potential, and the electron temperature are recovered by a fit of Eq.(1) to the data samples from the Langmuir electrode.

The main task of the MLP circuit is to set and maintain the optimal range of the bias voltages such that a complete $I - V$ characteristic can be reconstructed from current samples drawn by the Langmuir electrode at the three bias voltage states. In order to account for varying plasma conditions, the MLP dynamically updates the voltage states V^+ and V^- relative to the running average of the electron temperature samples over a 2 ms window such that $\Delta_V < 4\bar{T}_{e,2\text{ms}}$ holds. Here, $\Delta_V = V^+ - V^-$ and $\bar{T}_{e,2\text{ms}}$ denotes this running average of the electron temperature.

Large amplitude fluctuations of the boundary layer plasma on the other hand have a characteristic time scale of approximately $10\mu\text{s}$. During such transient events, the electron temperature may significantly exceed the running average, $T_e > \bar{T}_{e,2\text{ms}}$ such that the adjusted biasing voltage range may be insufficient to guarantee a precise fit on the true $I - V$ characteristic of a hypothetical Langmuir probe. But also events such as probe arcing may result in unphysical fit values.

A large body of experimental measurements suggest that the fluctuation statistics of the boundary plasma depend on the global parameters of the plasma discharge, such as line-averaged core plasma density and the magnetic geometry^{18,23,29-32}. Since the MLP biasing drive is agnostic to these circumstances, the accuracy and precision of data samples reported by the MLP may vary, depending on the plasma it samples. In order to accurately calculate lower order statistical moments of MLP data time series or distributions such as the probability distribution function or power spectral density, low-accuracy data samples should be discarded. However, if too many samples are discarded, these moments or distribution functions cannot be estimated with high statistical significance, due to the scarceness of available data points.

One way of pruning MLP data time series is to define valid ranges for the MLP parameters. Within these thresholds, samples are kept and out of bounds samples are to be discarded. A sensible boundary, or thresholds, needs to be low enough in order to reject samples with unphysically large fluctuation values. On the other hand, the threshold value needs to be large enough so that the accepted data points correctly capture the properties of the plasma fluctuations of the interrogated plasma. While measurements with a sufficient or insufficient biasing voltage range are readily identifiable, such a decision is ambiguous for a large fraction of other samples. In practice, it is often the case that several nearby Langmuir electrodes sample the plasma. Given that MLP samples may be quiet heterogeneous when operating on a small biasing voltage range, a threshold based method requires domain expertise and inevitably introduces biases.

Proposed Approach

The approach proposed here adopts simple thresholds to identify all *good* and *bad* measurements as a primer. This identification will be non-exhaustive, and will leave a large number of samples unclassified. From this, all uncertainty in the quality of the measurements will be treated with machine learning techniques which exploit statistical properties and regularities in the data. This approach allows to label unclassified data by making inference, as opposed to labing them using a complicated set of rules.

Specifically, we present an outlier classification framework based on an autoencoder (AE), a type of neural network that can be used to learn low-dimensional representations of arbitrary datasets. AEs will be trained using only good measurements samples so that they learn how to map them into low dimensional representations. Each dimension of the space induced by the AE mapping corresponds to a combination of features which best characterize the important features of *good* measurements. Those features are identified without making any *a-priori* assumption, but are automatically selected by the AE as the ones that are, *on average*, the most informative to describe the training samples. As a consequence, the numerical values of features in training samples will be similar and are mapped into a compact cluster in that low dimensional space.

AEs learn a representation of *good* measurement that are more *powerful*, due to the regularization constraints of the dimensionality reduction, and generalize better the samples. Evaluating similarities among samples represented in this new space is arguably more meaningful and reliable.

Once an AE is trained and the mapping to such a low dimensional space is learned, the unclassified samples will be processed. *Bad* measurements lack the characteristic features of *good* measurements and are expected to map onto vectors with a large distance to the cluster composed of *good* samples.

In order to identify a boundary between the representations of *good* and *bad* measurements, classifiers for vectorial data will be trained in this new space. Unclassified data samples are assigned a label based on which side of the decision boundary they fall.

The rest of this article is structured as follows: Sec. II describes measurements of plasma fluctuations by MLPs and discusses the structure of valid and invalid data at hand. Sec. III introduces AEs and describes their application for outlier detection in large datasets. The proposed classification method and its application to MLP data is described in Sec. IV. Sec. V discusses the performance of the proposed framework and Sec. VI gives a conclusion.

II. MEASUREMENTS OF PLASMA FLUCTUATIONS

Dedicated experiments with the goal to describe the statistics of fluctuation driven flows in the boundary plasma have been performed in the Alcator C-Mod tokamak^{33–36}. In these experiments, the boundary layer of an ohmically heated, lower single-null plasma discharge with a toroidal magnetic field strength of $B_T = 5.4$ T, was interrogated by four MLPs, connected to the electrodes of a Mach probe head, as shown in Fig. 2. The probe head was mounted on a linear servomotor probe drive system³⁷ and dwelled flush with plasma facing components at the outboard mid-plane location, as shown in Fig. 1. Extraordinarily long data time series of one second duration were sampled in stationary plasma discharge conditions with the goal to calculate the fluctuation statistics for the plasma with unprecedented accuracy.

The line-averaged core plasma density of the investigated discharge is $\bar{n}_e/n_G \simeq 0.6$, where n_G denotes the Greenwald density³⁰. For such high line-averaged core plasma densities, the average electron temperature in the far scrape-off layer plasma is below 10 eV. For lower \bar{n}_e/n_G , the scrape-off layer is commonly warmer²⁹. On the other hand, the MLPs registers order unity fluctuations of the electron temperature. That is, for such high \bar{n}_e/n_G and accompanying temperatures in the scrape-off layer, the MLP biasing drive operates at the limits of its design.

In order to assess the accuracy of fit parameters reported by the MLPs, they were compared among the four MLPs. Since the electrodes on the probe head are separated by approximately 2 mm, smaller than the characteristic size of structures in the boundary layer¹¹, it is expected that all four MLPs report similar fit parameters. Indeed, I_{sat} , T_e , and V_f fit parameters reported from the four MLPs are of comparable magnitude when the range of the biasing voltage states are large, $\Delta_V > 4T_e$. For the case where $\Delta_V \lesssim 4T_e$, the reported T_e fit parameters may show significant deviations. Operating with small bias voltage ranges, the relative fit error of the electron temperature, σ_{T_e}/T_e , is furthermore on average larger than for the case $\Delta_V > 4T_e$. The relative error on I_{sat} and T_e reported by the fit routine are correlated with a Pearson sample correlation coefficient of approximately one. The relative error on the floating potential is uncorrelated to the relative error of both, I_{sat} and T_e . While both I_{sat} and T_e are positive definite quantities, V_f may assume both positive as well as negative values. Thus, the relative error on the floating potential, σ_{V_f}/V_f , assumes large absolute values for small absolute values of V_f . This quantity is therefore not suitable to identify poor fits. Poor fits are identified by a large T_e value, a large relative fit error σ_{T_e}/T_e , and a small fit domain Δ_V/T_e .

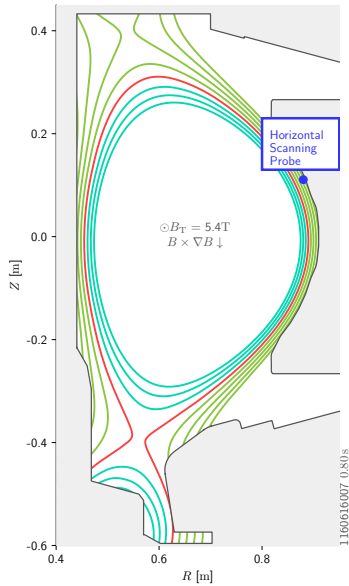


FIG. 1: The poloidal cross-section of the Alcator C-Mod tokamak. The blue dot marks the location where the MLPs sample the plasma. Green lines denote the open magnetic field lines, cyan lines denote the closed magnetic field lines. The red line separates the open field line region from the closed field line region. Material structures are shown in gray.

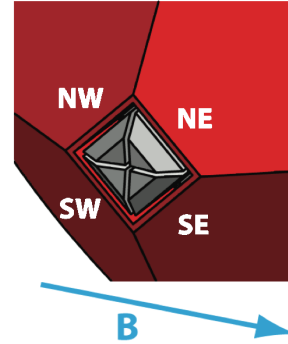


FIG. 2: The Mach probe head with four Langmuir electrodes, labelled "NE", "SE", "SW", and "SE", protruding from its top. The blue arrow denotes the direction of the local magnetic field.

Figure 3 shows data time series reported by the north-east and south-west MLP. The upper panel shows the electron temperature, the middle panel shows the relative error on T_e , and the lower panel shows the biasing voltage range. A large fraction of the samples feature small to moderate T_e values, together with small error proxies, that is a relative error $\sigma_{T_e}/T_e \lesssim 0.1$ and large biasing voltage range. Within these ranges, the fit parameters reported by the different MLPs are similar to one another, indicating that they are both, accurate and precise.

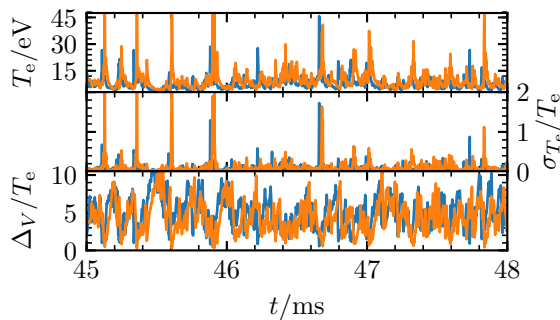


FIG. 3: Time series of the electron temperature (upper panel), the relative error on T_e (middle panel), and the range of the biasing voltages (lower panel), reported by the north-east (blue lines) and south-west (orange lines) MLP. Time series from the latter MLP are delayed by $20 \mu\text{s}$ for better visibility.

Large-amplitude fluctuations of the electron temperature appear intermittently in both time series. While the MLPs register them simultaneously, they report dissimilar T_e values, varying by up to 100%. Large amplitude fluctuations are furthermore associated with a large relative error σ_{T_e}/T_e and a small biasing voltage range. Comparing the appearance of large amplitude peaks sampled by the two MLPs, they may be grouped into several categories. One category are large amplitude peaks recorded by multiple MLPs but with disparate T_e values, for example at 45.1 ms,

at 45.4 ms, or at 45.9 ms. Another category are peaks where the MLPs report similar T_e values, for example at 45.25 ms or at 46.6 ms. Judging by the fit parameters reported by a single MLP, such peaks should be discarded. However, in the case where multiple MLPs report similar peaks, such samples may be retained. For the data at hand, electrode-averaged values may be used in combination with threshold values to identify samples which should be certainly kept or discarded. But for a majority of the data, such a simple classification may be ambiguous.

This broad range of variations under which large amplitude peaks are observed suggest that it is impractical to develop a comprehensive set of rules based on which to accept or reject reported peak amplitudes. In the following, we discuss how statistical inference can be used to derive such rules based from a priming sample of *good*, or accepted data.

Dataset description and threshold definition

Data time series of T_e , σ_{T_e}/T_e , and Δ_V , sampled by all four MLPs, are combined into a single dataset $\mathcal{X} = \{T_{e,p}, \sigma_{T_{e,p}}/T_{e,p}, \Delta_V/T_{e,p} \mid p \in \{\text{NE, SE, SW, NW}\}\}$. Each sample is a vector in \mathbb{R}^{12} corresponding to the individual measurements at a given time. We apply a simple threshold mechanism to label only a fraction of the original dataset. In particular, we identify *good* and *bad* samples, \mathcal{X}^g and \mathcal{X}^b , while the remaining samples are left unlabelled and referred as *uncertain* \mathcal{X}^u .

A fit reported by a single MLP is considered valid if T_e and σ_{T_e}/T_e are below a threshold value, and if Δ_V/T_e exceeds a threshold value. If the opposite conditions are true, the fit is considered invalid. If at least two MLPs report a valid fit, the vector is labelled *good* and assigned to \mathcal{X}^g . If at least two MLPs report an invalid fit, the vector is labelled *bad* and assigned to \mathcal{X}^b .

Table I lists three different sets of threshold values that are used for an a-priori partitioning of the data set \mathcal{X} . Depending on the threshold values used, the fraction of data points classified as *good*, *uncertain*, and *bad* varies. For example, the category *relaxed* denotes the partitioning that excludes the least amount of data from being categorized. Fits that report electron temperatures of up to 45 eV with a relative error of 0.75 over a range of $\Delta_V/T_e \geq 2.5$ are considered as valid. The fraction of *bad* and *uncertain* samples are listed in bottom row of tab. I. Using *relaxed* thresholds, approximately 20% of the data is unclassified, while approximately 40% of the data is labeled *uncertain* when using *strict* thresholds.

Quantity	relaxed	mid	strict
T_e/eV	45/50	40/45	35/40
σ_{T_e}/T_e	0.75/1.0	0.5/0.75	0.25/0.5
Δ_V/T_e	2.5/1.5	3.0/2.0	3.5/2.5
<i>uncertain/bad</i>	20.3% / 0.1%	30.0% / 0.1%	40.2% / 0.2%

TABLE I: Threshold values used for a-priori partitioning of the data. The first number gives the threshold for a poor fit, the second number gives the threshold for a good fit. The lowest row lists the fraction of data labeled as *uncertain* and *bad*.

In the following, we describe an approach where an AE is facilitated to identify data, which cannot be classified reliably by applying a threshold method.

III. AUTOENCODERS

AEs³⁸ are a particular class of neural networks, which received increasing interest in recent years^{39–41}. AEs can be used to learn unsupervised compressed, or lossy, representations of data, by training the network to map the input in a lower dimensional space through a bottleneck layer and then reconstruct the original input. In this way, the AE learns how to compress inputs, by retaining only the most important information necessary to yield a reconstruction that is as much accurate as possible⁴². Indeed, training AEs by minimizing a reconstruction error corresponds to maximizing the lower bound of the mutual information between input and the learned representation⁴³.

The bottleneck enforces a strong regularization that provides noise filtering, prevents the AE from learning trivial identity mappings (i. e., the identity function), and guarantees robustness to small changes in the inputs⁴⁴. Further regularization can be used to prevent overfitting on the training data and enhance the generalization properties of the representations. The most common regularizations are applying a ℓ_2 norm penalty to the weights learned network, and using dropout⁴⁵ to randomly drop connections between neurons at each iteration in the training phase. Dropout hinders couplings among neurons and therefore encourages to diversify the behavior of neurons.

In the training phase, an AE learns two functions at the same time. The first one is called *encoder* and provides a mapping from an input domain, \mathcal{X} , to a code domain, \mathcal{Z} , i. e. the latent representation space. Specifically, an input \mathbf{x} is represented as the output \mathbf{z} of the innermost layer in the AE. The second function, called *decoder*, implements a mapping from \mathcal{Z} back to \mathcal{X} . Fig. 4 depicts a standard AE architecture with a bottleneck.

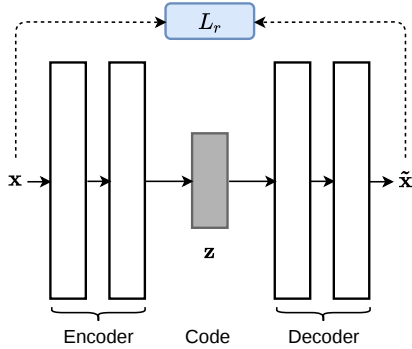


FIG. 4: Schematic representation of the AE architecture with a bottleneck. The encoder generates a low dimensional representation \mathbf{z} of the input \mathbf{x} . The AE is trained by minimizing the discrepancy (quantified by the loss L_r) between \mathbf{x} and its reconstruction $\tilde{\mathbf{x}}$ yielded by the decoder.

The encoding function $E(\cdot) : \mathcal{X} \rightarrow \mathcal{Z}$ and the decoding function $D(\cdot) : \mathcal{Z} \rightarrow \mathcal{X}$ of the AE define the following deterministic posteriors

$$\begin{aligned} \mathbf{z} &= E(\mathbf{x}) = p(\mathbf{z}|\mathbf{x}; \theta_E) \\ \tilde{\mathbf{x}} &= D(\mathbf{z}) = q(\tilde{\mathbf{x}}|\mathbf{z}; \theta_D), \end{aligned} \quad (4)$$

where θ_E and θ_D are the trainable parameters of the two functions; \mathbf{x} is the original input; \mathbf{z} is the code representation; $\tilde{\mathbf{x}}$ is the reconstruction of the input. The encoding and decoding function are usually implemented as two feed-forward neural networks, which are constrained to be symmetric. Each network consists of a stack of layers that can be dense, convolutional⁴⁶ or recurrent⁴⁷. Here, we focus only on dense layers that are implemented by an affine transformation followed by a non-linear activation function applied component-wise. Common activation functions are the sigmoid (logistic function, *tanh*), the maxout⁴⁸, and the rectified linear unit (ReLU).

Each layer contains a different number of processing units (neurons), which affects the capability of approximating a generic function. While a large number of layers and neurons per layer can provide more powerful modeling capabilities, the number of parameters increases with a consequent risk of overfit and a greater demand of computational resources. Therefore, an optimal configuration of the network should account for those contrasting properties.

The configuration of an AE with K layers in the encoder and decoder, respectively, can be suitably expressed as

$$\mathcal{C} = \{e_0, \dots, e_K, z, d_0, \dots, d_K\}, \quad (5)$$

where e_i and d_i define the number of neurons in the i -th layer of the encoder and the decoder. The size of the innermost layer is denoted by z and defines the dimension of the representation \mathbf{z} . As previously stated, we implement a symmetric encoder/decoder architecture by enforcing the following constraint $e_i = d_{K-i}$.

In order to minimize the discrepancy between the input and its reconstruction, the parameters θ_E and θ_D are adjusted by minimizing through stochastic gradient descent the following reconstruction loss

$$L = L_r + \lambda L_2 = \mathbb{E}_{\mathbf{x} \sim \mathcal{X}} [\|\mathbf{x} - \tilde{\mathbf{x}}\|^2] + \lambda (\|\theta_E\|^2 + \|\theta_D\|^2). \quad (6)$$

The term L_r minimizes the mean squared error between original inputs and their reconstructions, while L_2 penalizes large model weights. The hyperparameter λ controls the latter contribution to the total loss.

Besides the regularization parameter λ and the network configuration \mathcal{C} , other hyper-parameters that must be chosen by the user, or optimized by means of a validation procedure, are the following: the probability p_{drop} to drop neural connections during the training; the learning rate η used in stochastic gradient descent; the type of activation function implementing the non-linearities within each layer of the AE. We refer to the whole set of hyper-parameters as Γ_{ae} .

Outlier detection with Autoencoders

Outlier detection (also referred to as anomaly detection) is an important area of study in machine learning and is applied to several case-studies where non-nominal samples are scarce, noisy and not always available during training.

The objective of outlier detection procedures is to identify anomalous patterns, the outliers, in data that do not conform to an expected behavior⁴⁹.

Dimensionality reduction procedures, such as Principal Component Analysis (PCA), AEs and energy based models^{50,51} identify a subspace defined by the directions with largest variation among the nominal samples. While PCA can only capture variations that emerge from linear relationships in the data, more sophisticated models such as AEs account also for non-linear relationships. Therefore, AEs can identify a subspace defined by features that better characterize the nominal samples.

Anomaly detection methods based on dimensionality reduction rely on the assumption that anomalous samples do not belong to the subspace, learned during training, that contains nominal data. Indeed, the representations generated for samples of a new, unseen class will arguably fail to retain important characteristics, since the latent low-dimensional space induced by the AE does not span the most relevant features of the anomalous data. As direct consequences, the AE would yield large reconstruction errors for those samples and their low-dimensional representations would be significantly different and more scattered than for samples from the nominal class. This effect can be exploited to obtain an implicit separation between the classes in the code space, which can facilitate the separations of the two classes by a subsequent classifier.

Similar assumptions are reasonable for the MLP dataset at hand. As shown in Fig. 3, a large fraction of the MLP samples feature similar T_e fit values, together with σ_{T_e}/T_e and Δ_V values which indicate a reliable fit. These samples are considered as inliers and are used to train an AE. Having learned the important characteristics of inlier samples, hitherto unclassified samples will be mapped into the code space of the AE. Samples which do not share the important characteristics of the inlier samples should then be readily identifiable. In the following, we describe a classification framework that exploits this property of the data at hand to identify and separate outliers.

IV. PROPOSED CLASSIFICATION FRAMEWORK AND SELECTION OF MODEL PARAMETERS

The critical components of the proposed classification framework are the AE and the classifier used in the latent code space of the AE to discriminate between *good* and *bad* samples. Beside the trainable parameters, both components depend on a set of hyper-parameters whose tuning may affect the behavior of the whole framework. In the following, we discuss how the choice of a classifier and hyper-parameters for both, the AE and the classifier, results in different statistics of the inlier T_e data. In the last section, we discuss how the choice results in different statistics of the fluctuation driven heat flux. Since there is no ground truth available, that is, the real electron temperature of the plasma is unknown, no quantitative evaluation of the classification frameworks performance can be formulated. Instead, the design choices will be guided by the inferred biases of the filtered datasets for any given set of hyperparameters of the classification framework.

As discussed in Sec. III, the AE depends on several hyperparameters Γ_{AE} . In the following, we discuss the sensitivity of the mapping induced by the AE on them. Figure 5 shows the pipeline used for this task. For the sake of simplicity, we furthermore only consider the network layout $C^* = \{12, 2, 12\}$ at this point.

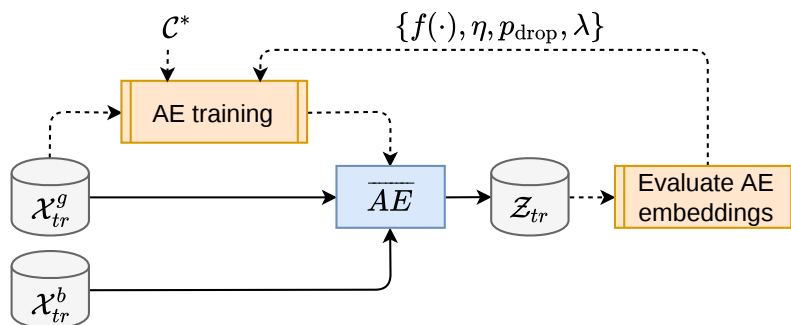


FIG. 5: Pipeline of the procedure to train the AE and select the optimal hyperparameters. \overline{AE} denotes a trained AE. C^* denotes an optimal layout of the AE that, that is assumed to be given for the task to identify the optimal hyperparameters.

5000 random elements from \mathcal{X}^g are used to train the AE. During training we observe little sensitivity to the hyperparameters p_{drop} , η , and λ . In the following, we select $p_{drop} = 10^{-1}$, $\eta = 10^{-2}$ and $\lambda = 10^{-3}$ as hyperparameters.

In feed-forward neural networks, each neuron computes the sum $y = \sum_i x_i w_i + b$, where x_i denotes the input from the previous layer, w_i denotes a weight and b denotes a bias. The weights and the bias are determined during the training phase. The output of each neuron is $f(y)$, which is called the activation function. The activation functions

considered here are

$$\begin{aligned}
 \text{sigmoid: } f(y) &= \frac{1}{1 + e^{-y}}, \\
 \text{tanh: } f(y) &= \frac{1 - e^{-2y}}{1 + e^{-2y}}, \\
 \text{ReLU: } f(y) &= \max(0, y), \\
 \text{Maxout: } f(y) &= \max_{r=1, \dots, 5} (\mathbf{w}_r y + \mathbf{b}).
 \end{aligned} \tag{7}$$

Figure 6 shows 1000 data points of the sets \mathcal{X}^g and \mathcal{X}^b each, mapped into the latent code space of AEs with these activation functions. The resulting sets \mathcal{Z}^g and \mathcal{Z}^b are colored in blue and orange respectively. Using tanh or sigmoid as activation functions, \mathcal{Z}^g and \mathcal{Z}^b appear difficult to separate. A large fraction of the *good* data points are mapped into a ellipsoid-shaped cluster for the tanh activation function whereas using sigmoids maps them into a hyperbola-shaped cluster. Data from \mathcal{Z}^g however show significant scatter around their respective clusters. *Bad* data are mapped onto band-like structures at the boundary of the image domain of the respective activation functions. Using Maxout or ReLU activation functions, the AE maps *good* data points into a narrow cluster and scatters *bad* data points along band-like structures. The image domain of these activation functions has no upper bound such that the separation of the *good* and *bad* data is larger for Maxout and ReLU activation functions than it is for tanh and sigmoids. The ReLU activation function can be considered as a special case of the Maxout function. Since the results obtained by those two activation functions are qualitatively comparable and since Maxout introduces additional parameters, in the following we only consider AEs using ReLU activation functions.

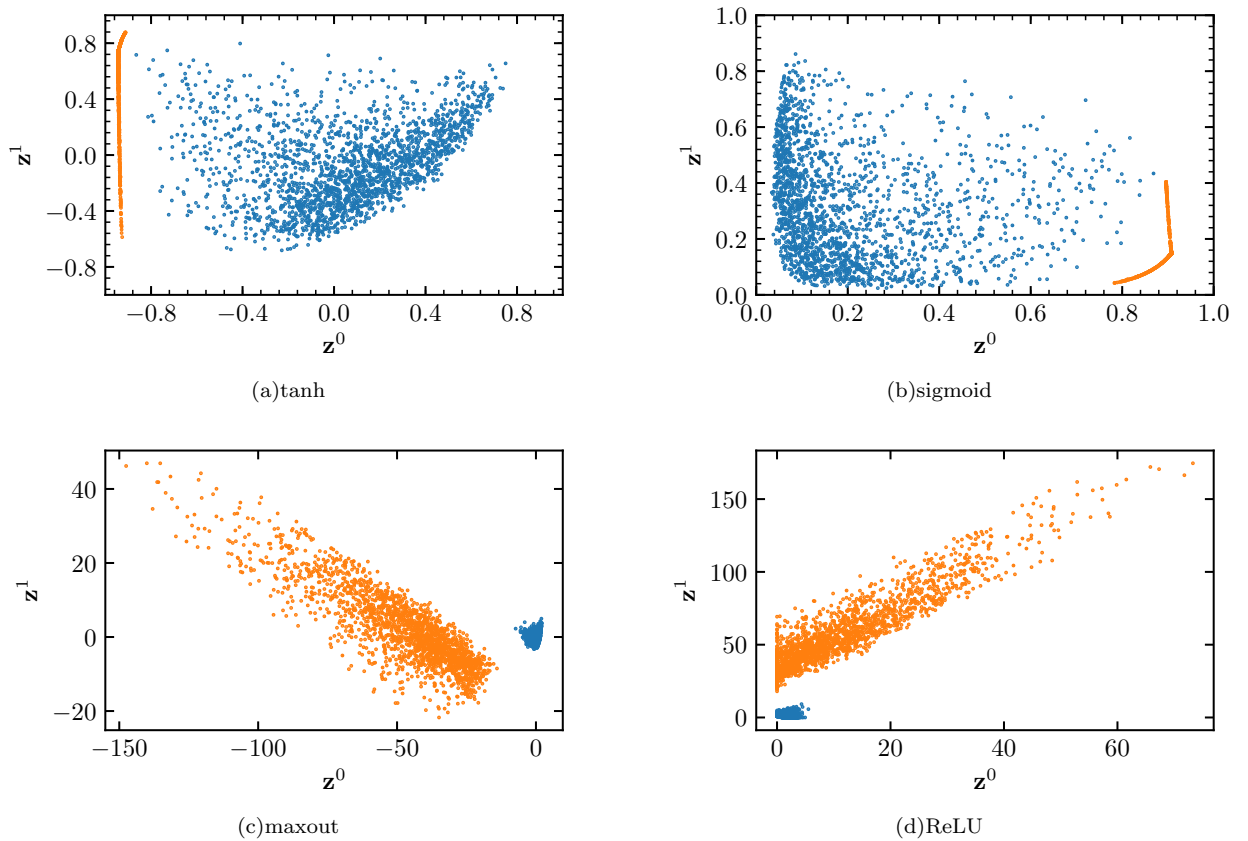


FIG. 6: *Good* (blue dots) and *bad* data (orange dots) in code space of AEs with $\mathcal{C} = \{12, 2, 12\}$ and different activation functions.

Codes produced by AEs with different layouts are qualitatively similar to those shown in Fig. 6. For AEs with $z = 3$, the data points usually feature only little variance along one of the three dimensions. That is, they cluster in a similar manner as they do for AEs with $z = 2$. Introducing an additional bottleneck layer in the AE, i. e. choosing $\mathcal{C} = \{12, 5, 2, 5, 12\}$, we observe a similar clustering of the data as is the case for $\mathcal{C} = \{12, 2, 12\}$. Postponing the effect

produced by different configurations of \mathcal{C} on the resulting statistics of the inlier T_e data, we continue by discussing the choice of a vector classifier in the code space \mathcal{Z} of the AE.

Once an AE is trained, it defines a mapping from the input domain \mathcal{X} into a unique, latent code space \mathcal{Z} . A classifier is trained on \mathcal{Z}^g and \mathcal{Z}^b and subsequently used to assign each $\mathbf{x} \in \mathcal{X}^u$ a label $\ell \in \{good, bad\}$. The set of all labels for the elements of \mathcal{X} is denoted as \mathcal{L} . A label $\ell \in \mathcal{L}$ denotes whether a sample will be considered as an inlier or outlier respectively. Such a classification introduces a bias, but with a validation procedure it is possible to evaluate how well it generalizes to unseen data and select the most suitable model accordingly.

Here we consider three standard classifiers for vectorial data: a support vector machine classifier (SVC), a nearest prototype classifier (PROT), and a so-called least-squares classifier (LS). The details of these classifiers are provided in the appendix.

To train a classifier, data is partitioned into a training and a validation set, \mathcal{Z}_{tr} and \mathcal{Z}_{val} . These sets contain only labelled samples: $\mathcal{Z}_{tr} = \{\mathcal{Z}_{tr}^g \cup \mathcal{Z}_{tr}^b\}$, $\mathcal{Z}_{val} = \{\mathcal{Z}_{val}^g \cup \mathcal{Z}_{val}^b\}$. The *good* training and validation data sets contain 1000 random data points each and the *bad* training and validation data sets contain approximately half the *bad* data each. \mathcal{Z}_{tr} is used to train the classifier, \mathcal{Z}_{val} is used to evaluate the generalization capability of the classifier. Fig. 7 provides a schematic depiction of the pipeline to train the classifier.

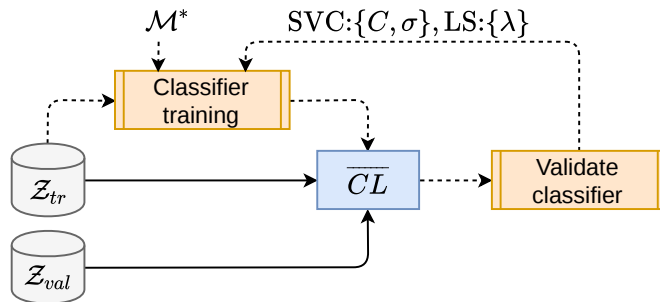


FIG. 7: Pipeline of the classifier training. The classifier \overline{CL} trained on \mathcal{Z}_{tr} is validated on \mathcal{Z}_{val} , to test its generalization capability and choosing the hyperparameters (such as C and σ in the SVM case). The model of the classifier $\mathcal{M} \in \{SVC, LS, PROT\}$ is assumed to be given at this stage.

The generalization capability of the classifier is quantified by the so-called *F1* score. It is defined as the harmonic mean of precision and recall, as calculated for the validation data, and assumes a value between zero and one. Precision is defined as the ratio of correctly classified outliers and all correctly classified data points. Recall is defined as the ratio of correctly classified outliers and the number of all data points classified as outliers. An *F1* score of zero describes a perfectly inaccurate classifier and a *F1* score of one describes a perfectly accurate classifier.

Figure 8 shows the decision boundaries learned by the three different classifiers as full lines. The training data used to learn the decision boundaries \mathcal{Z}_{tr} are indicated by the blue and orange dots. The SVC classifier, indicated by the purple line, draws a tight and curved decision boundary around \mathcal{Z}_{tr}^g , and the least-square classifier, the full brown line, draws a tight, linear boundary around \mathcal{Z}_{tr}^b . The decision boundary identified by the nearest prototype classifier, the red line, puts the decision boundary approximately half way between the class prototype. The *F1*-score of the classifiers are respectively given by 1.0, 1.0 and 0.97 for the shown data. This suggests that all three classifiers correctly label unseen data as either *good* or *bad*, that is, all three classifiers generalize equally well to unseen data.

Figure 9 shows an example of the classification process using the nearest prototype classifier. The leftmost panel shows the codes \mathcal{Z}_{tr}^g in blue dots and the codes \mathcal{Z}_{tr}^b in orange dots. The codes are clearly linearly separable, there is large leeway for placing the decision boundary. A nearest prototype classifier is fitted on \mathcal{Z}_{tr} , the prototypes μ_g and μ_b , as defined in Eq.(14), are depicted by a green and red dot respectively. This classifier is subsequently used to assign class labels to the validation data \mathcal{Z}_{val}^g and \mathcal{Z}_{val}^b , shown in the same color coding in the middle panel. Only few codes are mislabelled by the classifier, its *F1* score is approximately one. The rightmost panel shows the count of *uncertain* data codes \mathcal{Z}_u with assigned class labels.

Returning to the optimal configuration of the AE, we continue by discussing the statistics of all inlier samples $\mathcal{X}'^g = \mathcal{X}^g \cup \{\mathcal{X}^u | \mathcal{L}^u = good\}$ and outlier samples $\mathcal{X}'^b = \mathcal{X}^b \cup \{\mathcal{X}^u | \mathcal{L}^u = bad\}$, as identified by the proposed framework using the nearest prototype classifier. Figures 10(a) - 10(d) show the average electron temperature and the relative error on the electron temperature for different a-priori partitioning and different AE layouts. The numerals in the x-axis labels denote the AE layout \mathcal{C} and staggered plot markers refer to data from the individual MLPs “NE”, “SE”, “SW”, and “NW”. The error bars denote the sample standard variation. For the inlier samples, \overline{T}_e varies between 8 and 10 eV. This average shows little sensitivity to the used AE layout and the partition thresholds. There also appears a systematic difference in T_e as reported by the different probe heads. This may be due to shadowing of

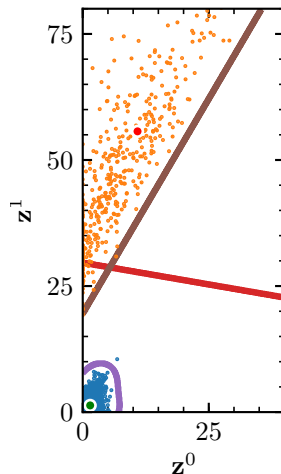


FIG. 8: Decision boundaries for a nearest prototype classifier (red line), a support vector machine classifier (purple line), and a least-square classifier (brown line). The red and green circle denote the class prototypes given by Eq.(14). The blue dots denote data from Z_{tr}^g and the orange dots denote data from Z_{tr}^b . The green and red circle denote the prototypes given by Eq.(14).

plasma flows, caused by the protruding probe head geometry. Plasma that is ballooned out at the outboard mid-plane will stream along the magnetic field lines. Following the field lines, it impinges first on the west electrodes. On the other hand, this discrepancy may also be due to a systematic error in the voltage measurements among electrodes due to slightly untuned capacitor bridges in the electronics.

The root-mean-square values of the T_e data are negligible for most \mathcal{X}^g , except for the $\mathcal{C} = \{12, 2, 12\}$ layout using *relaxed* partition thresholds and the $\mathcal{C} = \{12, 5, 2, 5, 12\}$ layout using *mid* partition thresholds. This effect is due to randomness in the used input data for the AE training. For these cases, significant root mean square values in \mathcal{X}'^g are seen. Data points classified as outliers, \mathcal{X}'^b , show average electron temperatures between approximately 30 and 50 eV. The relative error on these samples is given by approximately one. Again, the standard deviation of these samples is negligible in almost any AE configuration. This analysis suggests that the choice of a specific AE layout does not yield significantly different sample statistics of \mathcal{X}'^g . Therefore, we opt for the simplest configuration $\mathcal{C} = \{12, 2, 12\}$.

V. PERFORMANCE EVALUATION

In order to evaluate the performance of the proposed classification scheme, we continue by comparing the statistics of the final inlier data set as well as the lower order statistical moments of the heat flux, as computed from this data. The final inlier data sets are denoted by \mathcal{X}'^g , and are respectively identified using an SVC classifier, $\mathcal{X}'_{SVC}{}^g$, a least squares classifier, $\mathcal{X}'_{lsq}{}^g$, and a nearest prototype classifier, $\mathcal{X}'_{pro}{}^g$. We evaluate their performance by comparing the resulting statistics to those obtained from the entire dataset \mathcal{X} , the data without a-priori outliers, $\mathcal{X} \setminus \mathcal{X}^b$, as well as the data set of only a-priori inliners, \mathcal{X}^g . Fig. 11 illustrates the processing pipeline used to obtain these data sets. For the results presented here, an AE with ReLU activation functions and $\mathcal{C} = \{12, 2, 12\}$ is used.

Figure 12 shows the joint probability distribution function of the electron temperature and the relative error on the electron temperature as computed for these data sets. Here, T_e and σ_{T_e}/T_e denote the average value reported by all four MLPs. The entire data set \mathcal{X} , shown in Fig. 12(a), features many samples with small to medium T_e , associated with small to medium σ_{T_e}/T_e . A non-negligible fraction of the samples however feature large T_e values with $\sigma_{T_e}/T_e \gtrsim 1$. Considering only the good data, \mathcal{X}^g , shown in Fig. 12(b), all samples feature small T_e values and a negligible relative error. The joint PDF of the set $\mathcal{X} \setminus \mathcal{X}^b$ is similar to that of the set \mathcal{X} , but samples with $T_e \gtrsim 40$ eV are almost absent. This is due to the *strict* threshold values applied when removing \mathcal{X}^b .

Pruning the MLP data using an SVC classifier, $\mathcal{X}'_{SVC}{}^g$, shown in Fig. 12(d), the joint PDF appears similar in shape to the one for \mathcal{X}^g , Fig. 12(b). Only samples with $T_e \lesssim 15$ eV, associated with $\sigma_{T_e}/T_e \lesssim 0.3$ are present. Removing

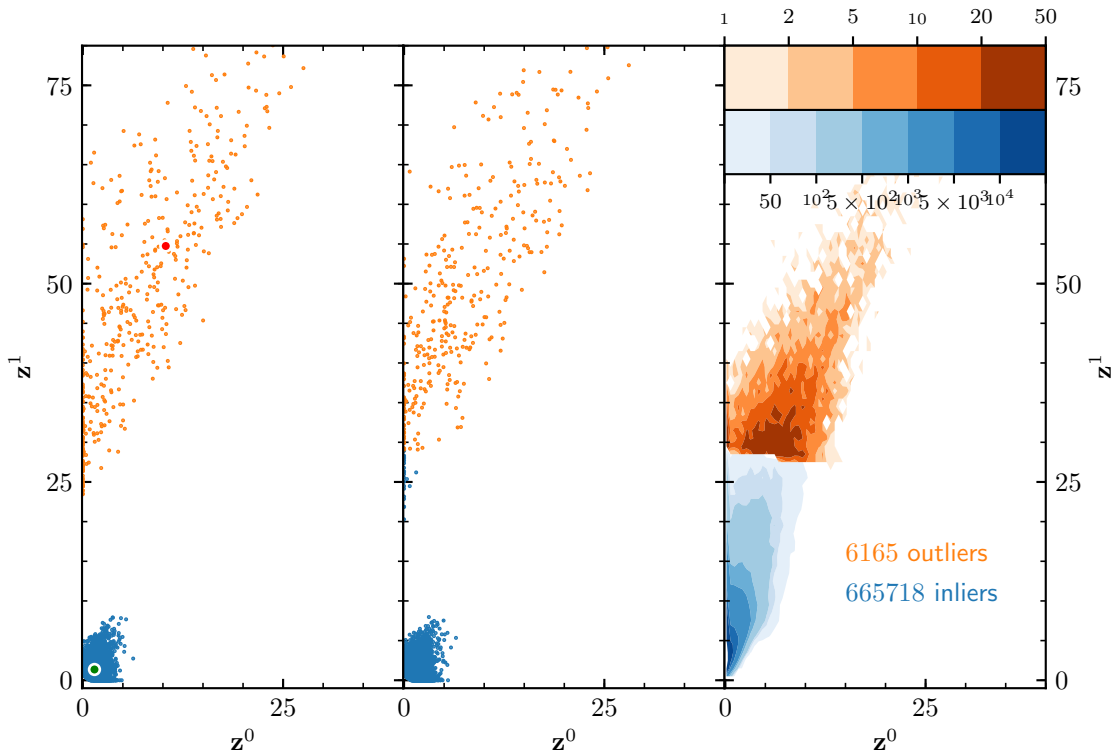


FIG. 9: Representation of the MLP data in code space of an AE with a single hidden layer of size $z = 2$. Blue denotes valid data, orange denotes invalid data points. The left and the middle panel respectively show training data \mathcal{Z}_{tr} and validation data \mathcal{Z}_{val} for the classifier Eq. (14). The right panel shows the count of data samples classified as either *good* (blue) or *bad* (orange).

outliers identified by the nearest prototype classifier, $\mathcal{X}'_{\text{pro}}{}^g$, shown in Fig. 12(e), several samples with $T_e \gtrsim 50$ eV are present. However, all samples feature relative errors less than approximately 0.75. Qualitatively, this joint PDF is similar to the joint PDF for $\mathcal{X} \setminus \mathcal{X}^b$, Fig. 12(c), except that samples with large σ_{T_e}/T_e are missing. Employing a least squares classifier, $\mathcal{X}'_{\text{lsq}}{}^g$, shown in Fig. 12(f), the resulting joint PDF is approximately aligned along an equi-probability contour of the joint PDF for \mathcal{X} , Fig. 12(a). There are no samples with $T_e \gtrsim 35$ eV and samples with $\sigma_{T_e}/T_e \gtrsim 1$ are also absent. Notably, samples $T_e \gtrsim 20$ eV with small σ_{T_e}/T_e are absent while the data set still includes samples with $T_e \gtrsim 20$ eV and large values of σ_{T_e}/T_e .

Figure 13 shows the mapping of the labels \mathcal{L}_{te} , as identified by the nearest prototype classifier into the time domain. The black lines and the red dots denote \mathcal{X}^g and \mathcal{X}^b respectively. Blue dots mark samples from \mathcal{Z}_{u} labelled $\ell = \textit{good}$, orange dots mark samples from \mathcal{Z}_{u} labelled $\ell = \textit{bad}$. The large amplitude fluctuations, at 45.1 ms, at 45.9 ms, and at

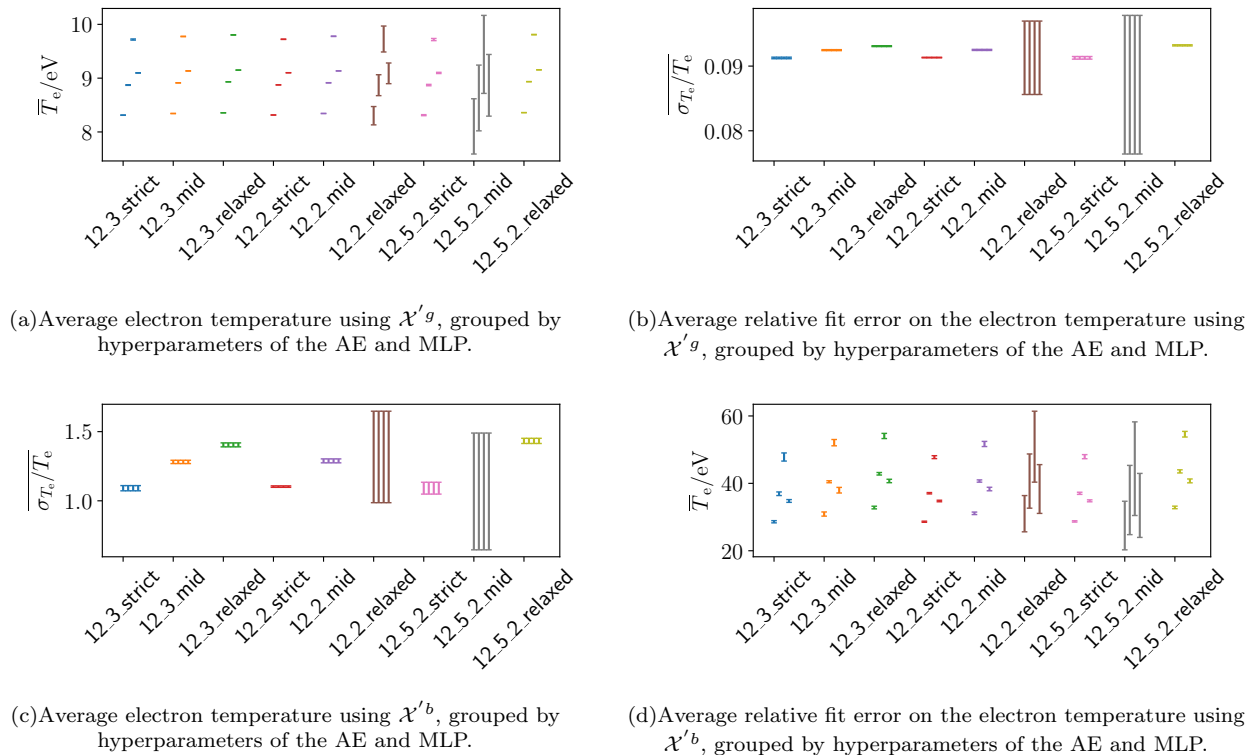


FIG. 10: Average electron temperature and relative error on the electron temperature for the inlier and outlier samples, as identified using different configurations of the AE and partition thresholds.

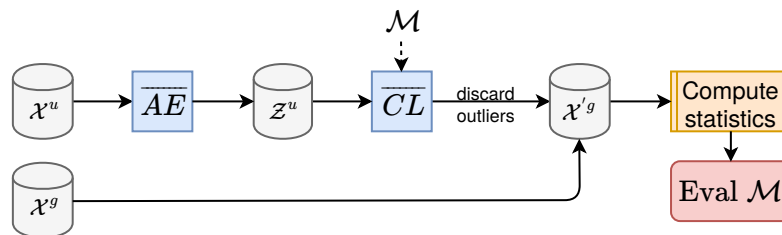


FIG. 11: Uncertain data \mathcal{X}_u are processed by \overline{AE} and \overline{CL} , trained as described in the previous section. To evaluate the classification model \mathcal{M} , we compare statistics on the classification results \mathcal{X}'^g .

46.6 ms are mostly classified as *good* data points. Notably, the peak at 46.2 ms is classified as *good*, even though the relative error and the range of the biasing voltage of this MLP are similar to the conditions of the preceding peak at 45.9 ms. This is due to the requirement that at least two MLPs need to report a invalid fit in order for a data point to be rejected.

A unique capability of Mirror Langmuir Probes is that they allow to study the fluctuation statistics of plasma flows driven by the electric drift. The heat flux impinging on plasma facing components is of special interest. It is comprised of a conduction driven part, $\hat{\Gamma}_{T,\text{cond}} = \tilde{U}\tilde{T}_e\langle n_e \rangle_{\text{mv}}/n_{e,\text{mrms}}$, a convection driven part $\hat{\Gamma}_{T,\text{conv}} = \tilde{U}\tilde{n}_e\langle T_e \rangle_{\text{mv}}/T_{e,\text{mrms}}$, and contributions from triple correlations $\hat{\Gamma}_{T,\text{tcor}} = \tilde{U}\tilde{n}_e\tilde{T}_e$. Here $\tilde{\cdot}$ denotes a quantity re-scaled by subtracting its moving average, $\langle \cdot \rangle_{\text{mv}}$, and dividing by its moving root-mean-square \cdot_{mrms} . In the following, we use a window length of 16384 elements for these filters³⁶.

Figure 14 shows the sample average and standard deviation for the three contributions of the radial heat flux, computed using different data sets and relative to the statistical moments computed ignoring a-priori outliers $\mathcal{X} \setminus \mathcal{X}^b$. The average heat fluxes and the standard deviations are largest when using the entire dataset \mathcal{X} . Using only good data, \mathcal{X}^g , yields averages and standard deviations less than 25% of the values calculated using $\mathcal{X} \setminus \mathcal{X}^b$. Notably, for this data the average radial heat flux due to triple correlations vanishes. Computing the moments using $\mathcal{X}'^g_{\text{SVC}}$, the

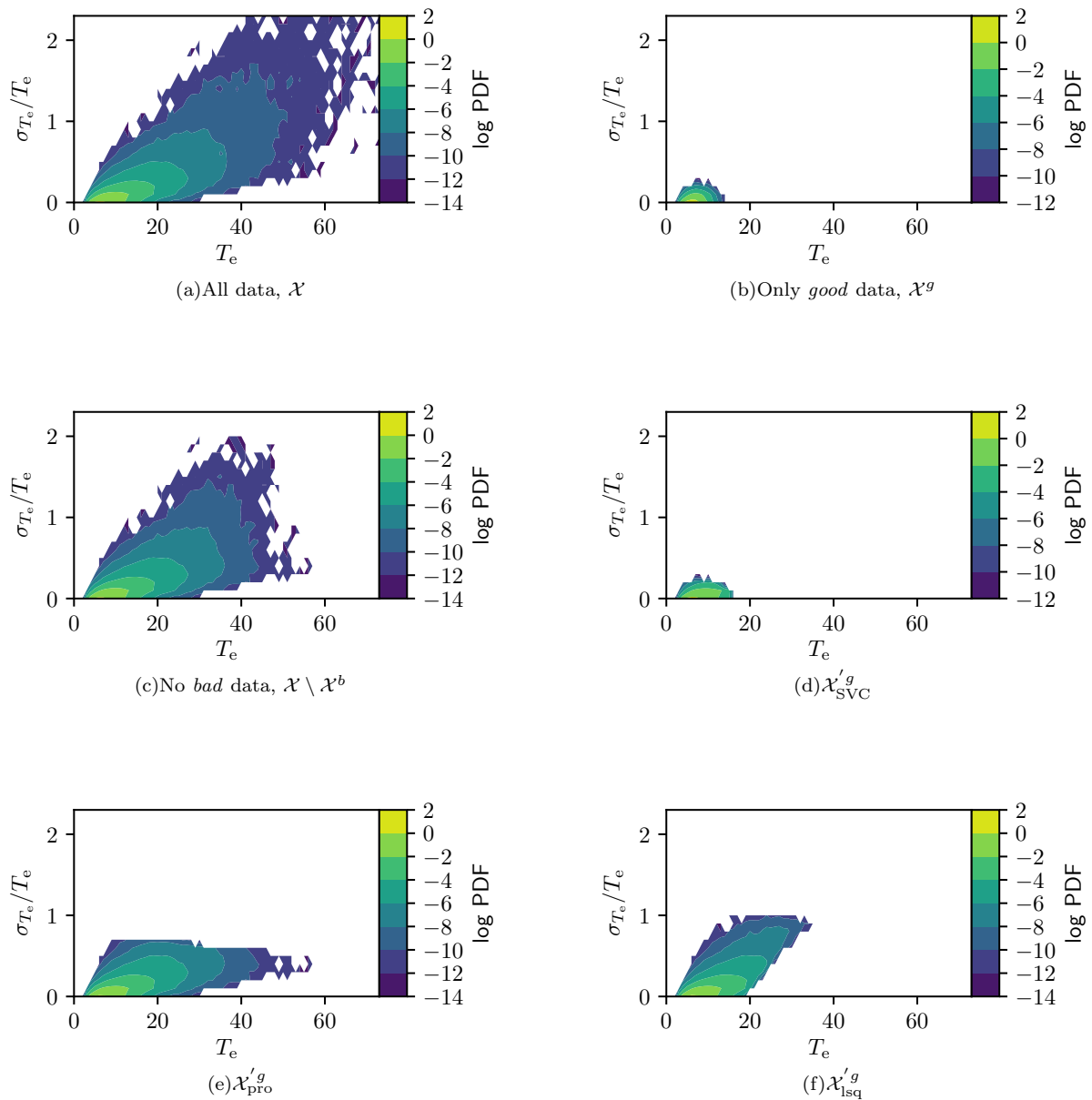


FIG. 12: Joint probability distribution function of the average electron temperature and the average relative error on the electron temperature after outliers have been removed by different methods.

average conductive and convective heat fluxes are approximately 50 and 60 percent of the reference values, while the average value of the contributions from triple correlations is approximately 20 percent.

Removing outlier data as identified by the nearest prototype classifier, $\mathcal{X}'_{\text{pro}}{}^g$, the average and root-mean-square values of the heat fluxes are approximately 85 – 95% of the reference value. Finally, using the least squares classifier results in statistical moments of the heat flux comparable to those using the reference case $\mathcal{X} \setminus \mathcal{X}^b$.

The difference in the sample averages and standard deviations of the various heat flux contributions can be related to the shape of the joint PDFs shown in Fig. 12. For this, we note that the heat flux is computed from T_e , n_e and V_p samples. The relative error on n_e is given by the geometric mean of the relative errors on I_{sat} and T_e . As discussed in Sec. II, σ_{T_e}/T_e and $\sigma_{I_{\text{sat}}}/I_{\text{sat}}$ are strongly correlated. That is, a larger relative error on σ_{T_e}/T_e implies a large relative error on the electron density.

Comparing the joint PDFs in Fig. 12, it is obvious that employing the different classifiers to remove outliers,

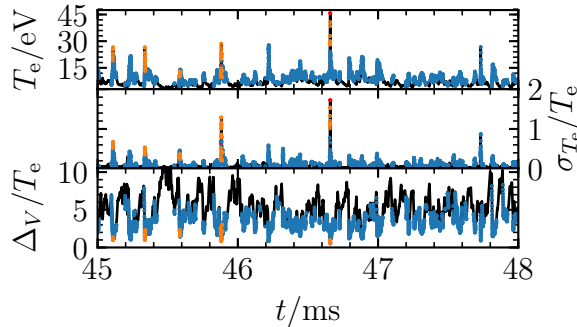


FIG. 13: Data time series of the north-east MLP (cf. blue lines in Fig. 3), overlaid with labels indicating classification of the data. Blue dots denote *good* samples, $\mathcal{X}'_{\text{pro}}{}^g$, orange dots denote *bad* samples, $\mathcal{X}'_{\text{pro}}{}^b$, and red crosses denote invalid samples \mathcal{X}^b , as classified by the prototype classifier using *strict* thresholds.

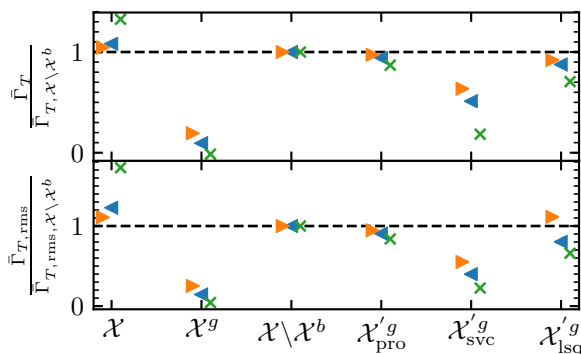


FIG. 14: Radial heat flux due to conduction (triangle left), convection (triangle right), and triple correlations (cross), as computed from the various data sets and relative to reference values computed using $\mathcal{X} \setminus \mathcal{X}^b$. The upper panel shows the sample average, the lower panel shows the sample standard deviation.

introduces slightly different biases into the inlier dataset.

VI. CONCLUSION

In conclusion, we propose a framework to classify outlier data in data time series sampled by a group of Mirror Langmuir probes in scrape-off layer plasmas. An autoencoder is trained to identify a low-dimensional representation of *good* fit data from this group of probes. In this space, each dimension corresponds to a combination of features which best characterizes the measurements. These are determined by the AE from the training data and without making any a-priori assumption about the data set at hand. Outlier data, which does not share the characteristics of *good* data, appears in a separable cluster in the space of the AE. Several classifiers are trained to separate outlier data in this space. With no ground truth available, the performance of the classifiers are evaluated by comparing the lower order statistical moments of the radial electron heat flux.

Using either a least squares or a nearest prototype classifier results in similar statistics of the radial heat flux as obtained when using a threshold classifier to identify outliers. Average contributions of the conductive and convective radial heat flux obtained by these classifiers fall approximately 3 and 14% percent below the values obtained by applying a threshold. On the other hand, the contribution due to triple correlations falls up to 40% below the value obtained from the thresholding method. These differences result from the different characteristics of the data points which are identified as outliers. While the least squares classifier places the decision boundary close to the outlier data cluster, the nearest prototype classifier places the decision boundary approximately equidistant to both clusters. That is, the least squares classifier gives a more relaxed outlier removal while the nearest prototype classifier has a

lower threshold. While neither method can be identified as the correct method to remove outliers from the data set, this study implies that not employing outlier removal may lead to heat fluxes, over-estimated by a significant amount.

The framework proposed here may also be adapted to other types of sensors than MLPs. The requirements for applying the method describes here are first, that any single sensor reports a physical quantity together with an uncertainty of that measurement. And second, any sensor in the group needs to sample roughly the same environment.

Acknowledgements

This work was supported with financial subvention from the Research Council of Norway under Grant No. 240510/F20 and the U.S. Department of Energy, Office of Science, Office of Fusion Energy Sciences, using User Facility Alcator C-Mod, under Award No. DE-FC02-99ER54512-CMOD. F. M. B. is founded by the Research Council of Norway under FRIPRO Grant No. 239844 “*Next Generation Learning Machines*”. R. K. acknowledges the generous hospitality of the MIT Plasma Science and Fusion Center where parts of this work were conducted.

Appendix

Classifiers are algorithms that assign a class label ℓ to new data, on the basis of previously seen training data with known class labels. For the case of two distinct classes, we assign $\ell = \pm 1$ to inliers and outliers respectively. In the following, we describe how labels ℓ_i for new data $\{x_i\}, x_i \in \mathbb{R}^d$ are retrieved using the classifiers used in this paper.

Support Vector Machine⁵²

A Support Vector Machines (SVM) learns a linear classifier in a kernel space,

$$\ell_i = g(x_i) = \text{sign}(\phi(w) \cdot \phi(x_i) + b), \quad (8)$$

induced by a usually non-linear kernel $\phi(w) \cdot \phi(x) = K(w, x)$. A typical choice for K is the radial basis function, defined as

$$K(x_i, x_j) = \exp\left(-\frac{\|x_i - x_j\|^2}{2\sigma^2}\right).$$

where σ is called the bandwidth of the kernel.

In order to train a SVM, the cost function

$$\phi^*(w) = \arg \min_{\phi(w)} \frac{1}{2} \|\phi(w)\|^2$$

is minimized under the constrain that $y_i(\phi(w) \cdot \phi(x_i) + b) \geq 1$. That is, the training data is taken to be only inlier data with $\ell_i = +1$.

The constraints can be included in the previous quadratic cost by using the Lagrangian multipliers,

$$L(\phi(w), b, \alpha) = \frac{1}{2} \|\phi(w)\|^2 - \sum_i \alpha_i (y_i(\phi(w) \cdot \phi(x_i) + b) - 1). \quad (9)$$

It follows that the weight vectors become a linear combination of the data points

$$\phi(w) = \sum_i y_i \alpha_i \phi(x_i), \quad (10)$$

and the classifier can be expressed as

$$g(x) = \text{sign}\left(\sum_i y_i \alpha_i \phi(x_i) \cdot \phi(x) + b\right) = \text{sign}\left(\sum_i y_i \alpha_i K(x_i, x) + b\right). \quad (11)$$

If we substitute (11) in (9), we obtain the following dual cost function

$$W(\alpha) = \sum_i \alpha_i - \frac{1}{2} \sum_{i,j} y_i y_j \alpha_i \alpha_j \phi(x_i) \cdot \phi(x_j) = \sum_i \alpha_i - \frac{1}{2} \sum_{i,j} y_i y_j \alpha_i \alpha_j K(x_i, x_j), \quad (12)$$

and the optimization now reads

$$\begin{aligned} \hat{\alpha} &= \arg \max_{\alpha} W(\alpha), \\ \text{such that } &\alpha_i \geq 0. \end{aligned} \quad (13)$$

Once the training is complete, new points are classified directly by applying (11).

Prototype classifier⁵³

Classification by means of simple a nearest prototype classifier, operates as follows. For each class c , a prototype is computed as

$$\mu_c = \frac{1}{|\{x_i\}|} \sum_i x_i. \quad (14)$$

The class label ℓ of an uncategorized data sample z is assigned as

$$\ell = \arg \min_c \|z - \mu_c\|^2 \quad (15)$$

This classifier does not depend on any hyperparameter and requires to maintain only the representative of each cluster to classify out-of-sample data. Due to its simplicity, this classifier cannot identify complex decision boundaries to separate samples of different classes.

Least square classifier

A classification function f is learned by minimizing the following quadratic cost

$$\min \frac{1}{N} \sum_{i=1}^N \|\ell_i - f(x_i)\|^2 + \lambda \|f\|^2 \quad (16)$$

where the first term penalize the discrepancy between the output class of the function and the known class of the training data. The second cost term instead encourage smoothness in the target function and is useful to prevent overfitting.

In the analysis presented here, we choose f to be a linear function

$$f(x) = Wx + b$$

whose parameters W and b are optimized according to (16).

A more flexible choice consists in using a kernel function to define f :

$$f(x) = \sum_{i=1}^N c_i K(x, x_i)$$

In this case, the objective of the optimization is to find the parameters c_i . This is done by modifying the quadratic loss in (16), which becomes

$$\min_{\mathbf{c}} \frac{1}{N} \sum_{i=1}^N \left\| y_i - \sum_{j=1}^N c_j K(x, x_j) \right\|^2 + \lambda \|\mathbf{c}^T \mathbf{K} \mathbf{c}\|^2. \quad (17)$$

* Electronic address: ralph.kube@uit.no

¹ J. Wesson, *Tokamaks* (Wesson, 2004), third edition, 2004 ed.

² G. Y. Antar, S. I. Krasheninnikov, P. Devynck, R. P. Doerner, E. M. Hollmann, J. A. Boedo, S. C. Luckhardt, and R. W. Conn, *Phys. Rev. Lett.* **87**, 065001 (2001), URL <http://link.aps.org/doi/10.1103/PhysRevLett.87.065001>.

- ³ G. Y. Antar, G. Counsell, Y. Yu, B. LaBombard, and P. Devynck, *Physics of Plasmas* **10**, 419 (2003), URL <http://link.aip.org/link/?PHP/10/419/1>.
- ⁴ Y. H. Xu, S. Jachmich, R. R. Weynants, and the TEXTOR team, *Plasma Physics and Controlled Fusion* **47**, 1841 (2005), URL <http://stacks.iop.org/0741-3335/47/i=10/a=014>.
- ⁵ J. P. Graves, J. Horacek, R. A. Pitts, and K. I. Hopcraft, *Plasma Physics and Controlled Fusion* **47**, L1 (2005), URL <http://stacks.iop.org/0741-3335/47/i=3/a=L01>.
- ⁶ O. E. Garcia, S. M. Fritzner, R. Kube, I. Cziegler, B. LaBombard, and J. L. Terry, *Phys. Plasmas* **20**, 055901 (2013).
- ⁷ J. L. Terry, S. J. Zweben, K. Hallatschek, B. LaBombard, R. J. Maqueda, B. Bai, C. J. Boswell, M. Greenwald, D. Kopon, W. M. Nevins, et al., *Physics of Plasmas* **10**, 1739 (2003), URL <http://link.aip.org/link/?PHP/10/1739/1>.
- ⁸ S. Zweben, R. Maqueda, D. Stotler, A. Keesee, J. Boedo, C. Bush, S. Kaye, B. LeBlanc, J. Lowrance, V. Mastrocola, et al., *Nuclear Fusion* **44**, 134 (2004), URL <http://stacks.iop.org/0029-5515/44/i=1/a=016>.
- ⁹ J. Terry, N. Basse, I. Cziegler, M. Greenwald, O. Grulke, B. LaBombard, S. Zweben, E. Edlund, J. Hughes, L. Lin, et al., *Nuclear Fusion* **45**, 1321 (2005), URL <http://stacks.iop.org/0029-5515/45/i=11/a=013>.
- ¹⁰ M. Agostini, J. Terry, P. Scarin, and S. Zweben, *Nuclear Fusion* **51**, 053020 (2011), URL <http://stacks.iop.org/0029-5515/51/i=5/a=053020>.
- ¹¹ R. Kube, O. Garcia, B. LaBombard, J. Terry, and S. Zweben, *Journal of Nuclear Materials* **438**, Supplement, S505 (2013), ISSN 0022-3115, URL <http://www.sciencedirect.com/science/article/pii/S0022311513001128>.
- ¹² G. Federici, C. Skinner, J. Brooks, J. Coad, C. Grisolia, A. Haasz, A. Hassanein, V. Philipps, C. Pitcher, J. Roth, et al., *Nuclear Fusion* **41**, 1967 (2001), URL <http://stacks.iop.org/0029-5515/41/i=12/a=218>.
- ¹³ D. Whyte, *Journal of Nuclear Materials* **390-391**, 911 (2009), ISSN 0022-3115, proceedings of the 18th International Conference on Plasma-Surface Interactions in Controlled Fusion Device, URL <http://www.sciencedirect.com/science/article/pii/S0022311509002621>.
- ¹⁴ S. edition, ed., *Principles of Plasma Diagnostics* (Cambridge University Press, 2002).
- ¹⁵ P. C. Stangeby, *The Plasma Boundary Of Magnetic Fusion Devices* (IoP Publishing, 2000).
- ¹⁶ V. Rohde, *Contributions to Plasma Physics* **36**, 109 (1996), ISSN 1521-3986, URL <http://dx.doi.org/10.1002/ctpp.19960360117>.
- ¹⁷ J. A. Boedo, D. Rudakov, R. Moyer, S. Krasheninnikov, D. Whyte, G. McKee, G. Tynan, M. Schaffer, P. Stangeby, P. West, et al., *Physics of Plasmas* **8**, 4826 (2001), URL <http://link.aip.org/link/?PHP/8/4826/1>.
- ¹⁸ J. A. Boedo, D. L. Rudakov, R. A. Moyer, G. R. McKee, R. J. Colchin, M. J. Schaffer, P. G. Stangeby, W. P. West, S. L. Allen, T. E. Evans, et al., *Physics of Plasmas* **10**, 1670 (2003), URL <http://link.aip.org/link/?PHP/10/1670/1>.
- ¹⁹ G. S. Kirnev, V. P. Budaev, S. A. Grashin, E. V. Gerasimov, and L. N. Khimchenko, *Plasma Physics and Controlled Fusion* **46**, 621 (2004), URL <http://stacks.iop.org/0741-3335/46/i=4/a=004>.
- ²⁰ O. E. Garcia, J. Horacek, R. A. Pitts, A. H. Nielsen, W. Fundamenski, J. P. Graves, V. Naulin, and J. J. Rasmussen, *Plasma Physics and Controlled Fusion* **48**, L1 (2006), URL <http://stacks.iop.org/0741-3335/48/i=1/a=L01>.
- ²¹ J. Horacek, J. Adamek, H. Müller, J. Seidl, A. Nielsen, V. Rohde, F. Mehlmann, C. Ionita, E. Havlíčková, and the ASDEX Upgrade Team, *Nuclear Fusion* **50**, 105001 (2010), URL <http://stacks.iop.org/0029-5515/50/i=10/a=105001>.
- ²² O. E. Garcia, R. Kube, A. Theodorsen, J.-G. Bak, S.-H. Hong, H.-S. Kim, the KSTAR Project Team, and R. Pitts, *Nuclear Materials and Energy* pp. – (2016), ISSN 2352-1791, URL <http://www.sciencedirect.com/science/article/pii/S2352179116301430>.
- ²³ R. Kube, A. Theodorsen, O. E. Garcia, B. LaBombard, and J. L. Terry, *Plasma Physics and Controlled Fusion* **58**, 054001 (2016), URL <http://stacks.iop.org/0741-3335/58/i=5/a=054001>.
- ²⁴ A. Theodorsen, O. E. Garcia, J. Horacek, R. Kube, and R. A. Pitts, *Plasma Physics and Controlled Fusion* **58**, 044006 (2016), URL <http://stacks.iop.org/0741-3335/58/i=4/a=044006>.
- ²⁵ H. Müller, J. Adamek, J. Horacek, C. Ionita, F. Mehlmann, V. Rohde, R. Schrittwieser, and A. U. Team, *Contributions to Plasma Physics* **50**, 847 (2010), ISSN 1521-3986, URL <http://dx.doi.org/10.1002/ctpp.201010144>.
- ²⁶ P. Verplancke, R. Chodura, J. Noterdaeme, and M. Weinlich, *Contributions to Plasma Physics* **36**, 145 (1996), <https://onlinelibrary.wiley.com/doi/pdf/10.1002/ctpp.19960360122>, URL <https://onlinelibrary.wiley.com/doi/abs/10.1002/ctpp.19960360122>.
- ²⁷ B. Labombard and L. Lyons, *Review of Scientific Instruments* **78**, 073501 (2007), ISSN 0034-6748.
- ²⁸ B. LaBombard, T. Goufopoulos, J. L. Terry, D. Brunner, E. Davis, M. Greenwald, and J. W. Hughes, *Physics of Plasmas* **21**, 056108 (2014), URL <http://dx.doi.org/10.1063/1.4873918>.
- ²⁹ B. LaBombard, R. L. Boivin, M. Greenwald, J. Hughes, B. Lipschultz, D. Mossessian, C. S. Pitcher, J. L. Terry, S. J. Zweben, and the Alcator C-Mod Group (Alcator Group), *Physics of Plasmas* **8**, 2107 (2001), URL <http://link.aip.org/link/?PHP/8/2107/1>.
- ³⁰ M. Greenwald, *Plasma Physics and Controlled Fusion* **44**, R27 (2002), URL <http://stacks.iop.org/0741-3335/44/i=8/a=201>.
- ³¹ O. E. Garcia, J. Horacek, R. A. Pitts, A. H. Nielsen, W. Fundamenski, V. Naulin, and J. J. Rasmussen, *Nuclear Fusion* **47**, 667 (2007), URL <http://stacks.iop.org/0029-5515/47/i=7/a=017>.
- ³² D. Carralero, G. Birkenmeier, H. Müller, P. Manz, P. deMarne, S. Müller, F. Reimold, U. Stroth, M. Wischmeier, E. Wolfrum, et al., *Nuclear Fusion* **54**, 123005 (2014), URL <http://stacks.iop.org/0029-5515/54/i=12/a=123005>.
- ³³ I. H. Hutchinson, R. Boivin, F. Bombarda, P. Bonoli, S. Fairfax, C. Fiore, J. Goetz, S. Golovato, R. Granetz, M. Greenwald, et al., *Physics of Plasmas* **1**, 1511 (1994), URL <http://dx.doi.org/10.1063/1.870701>.
- ³⁴ M. Greenwald, A. Bader, S. Baek, H. Barnard, W. Beck, W. Bergerson, I. Bespamyatnov, M. Bitter, P. Bonoli, M. Brookman, et al., *Nuclear Fusion* **53**, 104004 (2013), URL <http://stacks.iop.org/0029-5515/53/i=10/a=104004>.

- ³⁵ M. Greenwald, A. Bader, S. Baek, M. Bakhtiari, H. Barnard, W. Beck, W. Bergerson, I. Bespamyatnov, P. Bonoli, D. Brower, et al., *Physics of Plasmas* **21**, 110501 (2014), URL <https://doi.org/10.1063/1.4901920>.
- ³⁶ R. Kube, O. E. Garcia, A. Theodorsen, D. Brunner, A. Q. Kuang, B. LaBombard, and J. L. Terry, *Plasma Physics and Controlled Fusion* **60**, 065002 (2018), URL <http://stacks.iop.org/0741-3335/60/i=6/a=065002>.
- ³⁷ D. Brunner, A. Q. Kuang, B. LaBombard, and W. Burke, *Review of Scientific Instruments* **88**, 073501 (2017), <https://doi.org/10.1063/1.4990043>, URL <https://doi.org/10.1063/1.4990043>.
- ³⁸ G. Hinton and R. Salakhutdinov, *Science* (2006).
- ³⁹ D. P. Kingma and M. Welling, arXiv preprint arXiv:1312.6114 (2013).
- ⁴⁰ A. Makhzani, J. Shlens, N. Jaitly, I. Goodfellow, and B. Frey, arXiv preprint arXiv:1511.05644 (2015).
- ⁴¹ F. M. Bianchi, K. Ø. Mikalsen, and R. Jenssen, arXiv preprint arXiv:1710.07547 (2017).
- ⁴² Y. Bengio, *Foundations and trends® in Machine Learning* **2**, 1 (2009).
- ⁴³ P. Vincent, H. Larochelle, I. Lajoie, Y. Bengio, and P.-A. Manzagol, *Journal of Machine Learning Research* **11**, 3371 (2010).
- ⁴⁴ Y. Bengio, A. Courville, and P. Vincent, *IEEE Transactions on Pattern Analysis and Machine Intelligence* **35**, 1798 (2013), ISSN 0162-8828.
- ⁴⁵ N. Srivastava, G. E. Hinton, A. Krizhevsky, I. Sutskever, and R. Salakhutdinov, *Journal of machine learning research* **15**, 1929 (2014).
- ⁴⁶ J. Masci, U. Meier, D. Cireşan, and J. Schmidhuber, in *Artificial Neural Networks and Machine Learning – ICANN 2011*, edited by T. Honkela, W. Duch, M. Girolami, and S. Kaski (Springer Berlin Heidelberg, Berlin, Heidelberg, 2011), pp. 52–59, ISBN 978-3-642-21735-7.
- ⁴⁷ F. M. Bianchi, E. Maiorino, M. C. Kampffmeyer, A. Rizzi, and R. Jenssen, *Recurrent Neural Networks for Short-term Load Forecasting: An Overview and Comparative Analysis* (Springer, 2017).
- ⁴⁸ I. J. Goodfellow, D. Warde-Farley, M. Mirza, A. C. Courville, and Y. Bengio, *Proc. 30th International Conference on Machine Learning (ICML)* (2013).
- ⁴⁹ V. Chandola, A. Banerjee, and V. Kumar, *ACM computing surveys (CSUR)* **41**, 15 (2009).
- ⁵⁰ Z. Shuangfei, C. Yu, L. Weining, and Z. Zhongfei, in *Proceedings of The 33rd International Conference on Machine Learning* (2016), *Proceedings of Machine Learning Research*.
- ⁵¹ M. Sakurada and T. Yairi, in *Proceedings of the 2nd Workshop on Machine Learning for Sensory Data Analysis* (2014).
- ⁵² V. N. Vapnik, *IEEE transactions on neural networks* **10**, 988 (1999).
- ⁵³ J. C. Bezdek and L. I. Kuncheva, *International journal of Intelligent systems* **16**, 1445 (2001).